An optimized energy harvester for moving mass induced vibration

2011 Smart Mater. Struct. 20 055017

(http://iopscience.iop.org/0964-1726/20/5/055017)

Smart Mater. Struct. **20** (2011) 055017 (10pp) doi:10.1088/0964-1726/20/5/055017

An optimized energy harvester for moving mass induced vibration

Mingsian R Bai[1] **and Yao Kun Tsai**[2]

[1] Department of Power Mechanical Engineering, National Tsing-Hua University, 101 Sectoin 2, Kuang-Fu Road, Hsin-Chu 300, Taiwan
[2] Department of Mechanical Engineering, National Chiao-Tung University, 1001 Ta-Hsueh Road, Hsin-Chu 300, Taiwan

E-mail: msbai@pme.nthu.edu.tw

Received 30 December 2010, in final form 22 March 2011
Published 19 April 2011
Online at stacks.iop.org/SMS/20/055017

Abstract
This paper presents a piezoelectric energy harvester by which the vibration energy induced by a moving mass is converted to electrical energy through the piezoelectric effect. An electromechanically coupled finite element model (FEM) based on the Euler–Bernoulli beam theory is employed to estimate the electrical energy that can be generated by the energy harvester. The effects of mass ratio, beam length, travel time and load resistance on the energy output are examined. Experiments are conducted to verify the numerical model. The experimental results are in good agreement with the numerical prediction. In the design stage, the nonlinear conjugate gradient (CG) algorithm is applied for the calculation to maximize the energy throughput from the energy harvester. Results have shown that the harvested energy depends heavily upon the optimal choice of load resistance and travel time of the moving mass. In addition, the longer the beam or the higher the mass ratio, the higher the energy throughput that can be achieved.

(Some figures in this article are in colour only in the electronic version)

Nomenclature

A	cross-section area
a	length of the beam element
$\mathbf{C}$	damping matrix
$\mathbf{c}$	elastic matrix
c_{p}	capacitance of the piezoelectric ceramic
$\mathbf{D}$	global degree of freedom vector
$\mathbf{d}$	vector of nodal degree of freedom
d_{31}	piezoelectric constant
$\mathbf{E}$	dielectric displacement
$\mathbf{e}$	elastic constant matrix
E	Young's modulus
EI	bending rigidity
$\mathbf{f}$	vector of external force
J	cost function
$\mathbf{K}$	stiffness matrix
L	beam length
$\mathbf{M}$	mass matrix
m	moving mass
$\mathbf{N}$	raw shape function vector of transverse displacement
N	shape function of longitudinal displacement
n	number of element
R_{L}	electrical resistive load
$\mathbf{S}$	strain vector
$\mathbf{s}$	vector of design parameter
$\mathbf{T}$	stress vector
$\mathbf{\Gamma}$	dielectric vector
T	kinetic energy
T_{f}	resonant period (reciprocal of the resonant frequency)
t_1	distance between the bottom of the piezoelectric layer and the neutral axis
t_2	distance between the top of the piezoelectric layer to the neutral axis
t_{b}	thickness of the substrate layer
t_z	thickness of the piezoelectric layer
$\mathbf{U}$	raw shape function vectors for longitudinal displacement
U	shape function for longitudinal displacement
u	longitudinal displacement

V_T	strain energy
V	volume
v_p	voltage output
W_b	width of the beam
W_e	electrical energy
w	lateral displacement
α	damping coefficient
$\alpha_{C(i)}$	step size of the nonlinear CG
β	damping coefficient
β_m	mass ratio
Θ	electromechanical coupling matrix
θ	rotation on y-axis
ρ	density
δ	dynamic deflection of the beam subjected to the moving mass
τ	total travel time of the mass moving from the left end to the right end
Subscript	
b	substrate layer property
z	piezoelectric layer property
Superscript	
E	parameters are measured under constant electric field
S	parameters are measured under constant strain

1. Introduction

In recent years, the idea of energy harvesting has received much research attention due to its prospective applications in self-powered microsystems. Examples of such systems are wireless sensors, biomedical implants, military monitoring devices, structure-embedded instrumentation, remote controllers, calculators, watches, etc. Various approaches of electromechanical transduction such as electromechanical transduction [1], electrostatic transduction [2, 3], piezoelectric transduction [4], magnetostrictive transduction [5] and thermoelectric transduction [6] have been exploited to serve as alternative energy sources. In the last decade, numerous approaches to vibration-based energy harvesting have been suggested [4, 7, 8]. Piezoelectric transduction has played a key role among these studies for a wide spectrum of vibration-based energy harvesters. This is mainly due to the unique ability of piezoelectric materials to efficiently convert mechanical energy into electrical energy. Various approaches to modeling energy harvesters have been suggested in literature. Umeda *et al* [9] proposed an equivalent circuit based on a single-degree-of-freedom (SDOF) model consisting of a mass, a spring and a damper. Roundy *et al* [10], du Toit *et al* [11] and Ajitsaria *et al* [12] all employed the SDOF model for analysis. Although the SDOF model provides useful insights into harvesting systems, it is essentially an approximation limited to modeling a single mode of vibration, which tends to overlook important aspects such as dynamic mode shapes, strain distribution and electrical responses. Erturk *et al* [13] provided necessary modifications to the electromechanical modeling. Other researchers tried to improve the models. Hagood *et al* [14] conducted an electromechanical analysis using the Rayleigh–Ritz approach and the generalized Hamilton principle. The discrete model obtained using this approach provides a more accurate approximation than the SDOF model. Lu *et al* [15] introduced a single-mode model into the piezoelectric constitutive relation to calculate the electric displacement. The relation between the electrical output and the mechanical mode shape is established in this work. Erturk and Inman [16] derived an analytical solution for a cantilevered piezoelectric harvester on the basis of Euler–Bernoulli beam theory. Their analysis has taken internal strain rate damping and external air damping into account. Marqui *et al* [17] presented a finite element model to predict the electrical power output from a piezoelectric plate. A generator wing spar with embedded piezoelectric ceramics is designed using optimization techniques. Traditional vibration-based piezoelectric energy harvesters are in general designed by matching their fundamental natural frequency and the base excitation frequency. Challa *et al* [18] proposed a resonance frequency tunable energy harvester using magnetic force. The magnets are placed at the free end of the cantilevered piezoelectric beam, where the attractive and repulsive magnetic forces can be exerted on each side of the beam to adjust the natural frequency. Wickenheiser and Garcia [19] proposed a magnetic rectification approach to make the energy harvesting performance more robust against broadband random excitation at the base. The system is most effective when the driving frequencies are well below its fundamental frequency, enabling a more compact design over traditional systems.

In contrast to traditional harvesters that take advantage of base excitation, the present work proposes a unimorph piezoelectric beam device aimed at harvesting energy from moving mass excitation [20]. In the literature, many researchers have attempted various techniques to harvest vibration energy efficiently and effectively. Most designs are focused on a single resonance frequency. Therefore, their performance is limited to a narrow range of frequencies. In order for these energy harvesting devices to be commercially viable in practical applications, they have to function over a wide range of frequencies without sacrificing energy output. By scavenging energy from the environment, the transient response of the energy output can be more important than excitation at a single frequency. That motivates the development of an energy harvester for moving mass induced vibration. Potential applications based on this principle are, for example, bridges, road bumps, railways, mass rapid transit (MRT), overhead cranes and toll stations. The electromechanical equations of motion are derived for transverse vibrations based on the Euler–Bernoulli beam theory. The resulting FEM is solved via the Newmark-β method [21]. In order to maximize the harvested energy, optimization based on the nonlinear conjugate gradient (CG) algorithm [22, 23] is employed to determine the optimum travel time of the moving mass and the optimum load resistance for a specified beam length. The optimum parameters of the present system are discussed in detail. In addition, the effects of velocity, acceleration, mass ratio and beam length variation are also examined.

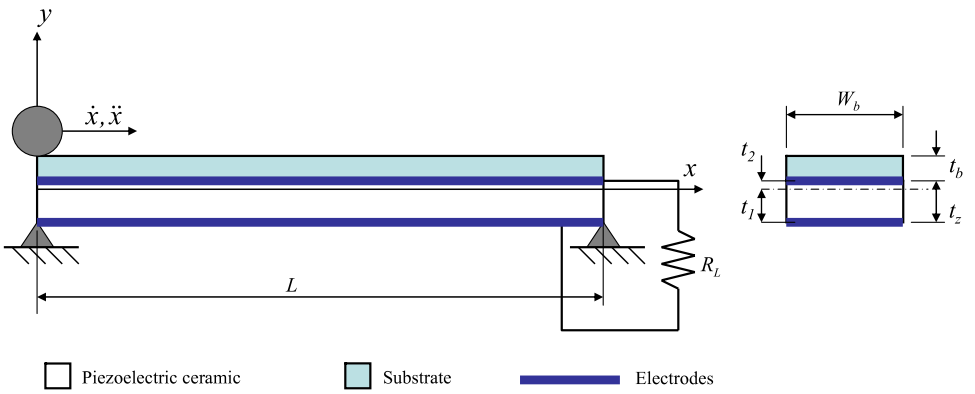

Figure 1. The simply supported piezoelectric energy harvester for moving mass induced vibration.

2. Finite element models of a piezoelectric energy harvester

In this section, the equations of motion for the piezoelectric energy harvester are derived based on the Euler–Bernoulli beam theory, followed by the electromechanical FEM formulations.

2.1. Linear piezoelectric constitutive relationships

The energy method in conjunction with the FEM is employed to derive the equations of motion for the energy harvester. The linear-electroelastic constitutive relation for piezoelectric ceramic materials is [24]

$$\begin{Bmatrix} \mathbf{T} \\ \mathbf{\Gamma} \end{Bmatrix} = \begin{bmatrix} \mathbf{c}^{\mathrm{E}} & -\mathbf{e}^{\mathrm{T}} \\ \mathbf{e} & \boldsymbol{\varepsilon}^{\mathrm{S}} \end{bmatrix} \begin{Bmatrix} \mathbf{S} \\ \mathbf{E} \end{Bmatrix}, \tag{1}$$

where **T** is the mechanical stress vector, **Γ** is the electric displacement vector, **S** is the mechanical strain vector, and **E** is the electric field vector. Matrices **c**, **e** and $\boldsymbol{\varepsilon}$ are the elastic stiffness matrix, the piezoelectric parameter matrix, and permittivity. Superscripts E and S indicate that the parameters are measured under constant electric field and constant strain conditions.

2.2. Modeling a simply supported piezoelectric beam

Consider a simply supported beam subjected to a moving mass load, as shown in figure 1. The lateral displacement w is interpolated using cubic polynomials of the physical coordinates, whereas the longitudinal displacement is interpolated by linear polynomials. An Euler–Bernoulli beam element with two nodes and three degrees of freedom per node shown in figure 2 is used. The displacement fields within an element are interpolated as [25]

$$w = \mathbf{N}\mathbf{d}, \qquad u = \mathbf{U}\mathbf{d}, \tag{2}$$

where

$$\begin{aligned} \mathbf{N} &= [\,0 \quad N_1 \quad N_2 \quad 0 \quad N_3 \quad N_4\,], \\ \mathbf{U} &= [\,U_1 \quad 0 \quad 0 \quad U_2 \quad 0 \quad 0\,], \\ \mathbf{d} &= [\,u_1 \quad w_1 \quad \theta_1 \quad u_2 \quad w_2 \quad \theta_2\,]^{\mathrm{T}}, \end{aligned} \tag{3}$$

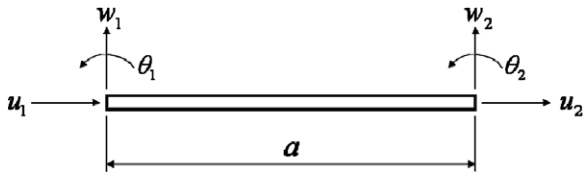

Figure 2. A two-node Euler–Bernoulli beam element with three degrees of freedom per node.

and

$$\begin{aligned} N_1 &= 1 - (3ax^2 - 2x^3)/a^3, \\ N_2 &= (a^3x - 2a^2x^2 + ax^3)/a^3, \\ N_3 &= (3ax^2 - 2x^3)/a^3, \qquad N_4 = (-a^2x^2 + ax^3)/a^3, \\ U_1 &= (a - x)/a, \qquad U_2 = x/a, \end{aligned} \tag{4}$$

$\theta = \frac{\partial w}{\partial x}$ and u denote the cross-section rotation and longitudinal displacement, respectively; **N** and **U** denote 1×6 shape function vectors for transverse displacement and longitudinal displacement, respectively; **d** is the vector of the nodal degrees of freedom; a is the length of the beam element; and x is the coordinate along the longitudinal direction of the beam element. Thus, the kinetic energy, strain energy and electrical energy for the piezoelectric harvester can be expressed as

$$T = \frac{1}{2}\int_{Vb} \rho_b \dot{\mathbf{D}}^{\mathrm{T}}\mathbf{D}\,\mathrm{d}V_b + \frac{1}{2}\int_{Vz} \rho_z \dot{\mathbf{D}}^{\mathrm{T}}\mathbf{D}\,\mathrm{d}V_z + \frac{1}{2}m\left(\frac{\partial u}{\partial t}\right)^2, \tag{5}$$

$$V_{\mathrm{T}} = \frac{1}{2}\int_{V_b} \mathbf{S}^{\mathrm{T}}\mathbf{T}\,\mathrm{d}V_b + \frac{1}{2}\int_{V_z} \mathbf{S}^{\mathrm{T}}\mathbf{T}\,\mathrm{d}V_z + \frac{1}{2}\int_{V_b} E_b\frac{\partial u}{\partial x}\,\mathrm{d}V_b + \frac{1}{2}\int_{V_z} E_z\frac{\partial u}{\partial x}\,\mathrm{d}V_z, \tag{6}$$

$$W_{\mathrm{e}} = \tfrac{1}{2}\int_{V_z} \mathbf{E}^{\mathrm{T}}\mathbf{\Gamma}\,\mathrm{d}V_z, \tag{7}$$

where **D** denotes the vector of global degree of freedom, m_b, and m_z are the mass per unit length for the substrate and the piezoelectric ceramic, respectively, ρ_b and ρ_z are the mass per unit volume for substrate and piezoelectric ceramic,

respectively, E_b and E_z are Young's moduli for substrate and piezoelectric ceramic, respectively, and m is the mass of the moving object. The force acted by the moving load can be written as

$$f = mg - m\ddot{w}, \tag{8}$$

where

$$\ddot{w}(x,t) = \frac{\partial^2 w}{\partial x^2}\dot{x}^2 + 2\frac{\partial^2 w}{\partial x \partial t}\dot{x} + \frac{\partial w}{\partial x}\ddot{x} + \frac{\partial^2 w}{\partial t^2}. \tag{9}$$

By using the Lagrange equation, the electromechanical equations of motion can be written in a matrix form as

$$\mathbf{M}\ddot{\mathbf{D}} + \mathbf{C}\dot{\mathbf{D}} + \mathbf{K}\mathbf{D} - \mathbf{\Theta}v_\mathrm{p} = \mathbf{f}, \tag{10a}$$

$$c_\mathrm{p}\dot{v}_\mathrm{p} + \frac{v_\mathrm{p}}{R_L} + \mathbf{\Theta}^\mathrm{T}\dot{\mathbf{D}} = 0, \tag{10b}$$

where

$$\mathbf{M} = \sum_{k=1}^{n}\left\{\int_0^a (m_b + m_z)\mathbf{N}^\mathrm{T}\mathbf{N}\,\mathrm{d}x + \int_0^a (m_b + m_z)\mathbf{U}^\mathrm{T}\mathbf{U}\,\mathrm{d}x + \int_0^a (\rho_b + \rho_b) I \mathbf{N}_x^\mathrm{T}\mathbf{N}_x\,\mathrm{d}x + m\mathbf{U}^\mathrm{T}\mathbf{U} + m\mathbf{N}^\mathrm{T}\mathbf{N}\right\}_k, \tag{10c}$$

$$\mathbf{C} = \sum_{k=1}^{n}\{\mathbf{C}_\mathrm{s} + 2m\mathbf{N}^\mathrm{T}\mathbf{N}_x\dot{x}\}_k, \tag{10d}$$

$$\mathbf{K} = \sum_{k=1}^{n}\left\{\int_0^a EI\mathbf{N}_{xx}^\mathrm{T}\mathbf{N}_{xx}\,\mathrm{d}x + \int_0^a EA\mathbf{U}_x^\mathrm{T}\mathbf{U}_x\,\mathrm{d}x + m\mathbf{N}^\mathrm{T}\mathbf{N}_{xx}\dot{x}^2 + m\mathbf{N}^\mathrm{T}\mathbf{N}_x\ddot{x}\right\}_k, \tag{10e}$$

$$\mathbf{\Theta} = \sum_{k=1}^{n}\left\{\frac{d_{31}E_z W_b(t_1^2 - t_2^2)}{2t_z}\int_0^a \mathbf{N}_{xx}^\mathrm{T}\,\mathrm{d}x\right\}_k, \tag{10f}$$

$$\mathbf{f} = \sum_{k=1}^{n}\{\mathbf{N}^\mathrm{T}mg\}_k. \tag{10g}$$

The matrices $\mathbf{M}$, $\mathbf{C}$, and $\mathbf{K}$ denote the structural mass, damping, and stiffness matrices of the beam; $\mathbf{\Theta}$ is the electromechanical coupling matrix; $\mathbf{f}$ is the external load vector; structure damping $\mathbf{C}_\mathrm{s} = \alpha\mathbf{M} + \beta\mathbf{K}$ is assumed [26]. A is the cross-section area and EI is the bending rigidity [27]. v_p, c_p, and R_L represent the voltage output, capacitance of the piezoelectric ceramic, and resistive load. The parameter d_{31} is the piezoelectric constant, subscripts 1 and 3 denote the directions coincident with x and y directions, respectively. W_b is the width of the beam; t_z is the thickness of the piezoelectric layer; t_1 is the distance between the bottom of the piezoelectric layer and the neutral axis; t_2 is the distance between the top of the piezoelectric layer to the neutral axis (figure 1); and n is the number of elements. It should be noted that the matrices associated with the moving mass in equations (10*c*), (10*d*) and (10*e*) are null matrices except for those corresponding to the nodal displacements of the element on which the mass is moving.

3. Optimal design of the piezoelectric harvester

In order to maximize the harvested energy, the nonlinear conjugate gradient (CG) algorithm is employed to determine the design parameters appropriate for the energy harvester. It can be regarded as an intermediate approach between the steepest descent method and Newton's method. The basis for the nonlinear conjugate gradient method is to effectively apply the linear conjugate gradient method, where the residual is replaced by the gradient. A model objective function is never explicitly formed and it is always combined with a 'line search' method. The advantage of the conjugate gradient method is that it requires relatively little memory space for large-scale problems, virtually no numerical linear algebra, and no need to compute Hessian of objective function. The computation in each step can be accomplished within a very short time. This method has proved to be extremely effective in dealing with general objective functions and is considered among the best general purpose optimization methods currently available.

The basic idea of the CG method is that the searching directions have to be orthogonal [22] to all previous search directions. The nonlinear CG algorithm can be derived from the linear algorithm by considering three aspects: the recursive formula for the residual calculation cannot be used; to compute the step size α_C becomes more complicated; various choices for β_C are available. The nonlinear CG procedure can be formulated by maximizing the cost function $J(\mathbf{s})$ of the design parameter vector $\mathbf{s} = \mathbf{s}(s_1, s_2, \ldots, s_n)$:

(1) Choose initial gradient $\mathbf{h}_{(0)} = \mathbf{r}_{(0)} = [\frac{\partial J(\mathbf{s}_{(0)})}{\partial s_1} \ \ldots \ \frac{\partial J(\mathbf{s}_{(0)})}{\partial s_n}]^\mathrm{T}$.
(2) Find the step size $\alpha_{\mathrm{C}(i)}$ that maximizes $J(\mathbf{s}_{(i)} + \alpha_{\mathrm{C}(i)}\mathbf{h}_{(i)})$ by using the golden section search with parabolic interpolation (GSS–PI) [28].
(3) Calculate the gradient for the next step. $\mathbf{s}_{(i+1)} = \mathbf{s}_{(i)} + \alpha_{\mathrm{C}(i)}\mathbf{h}_{(i)}$, $\mathbf{r}_{(i+1)} = J'(\mathbf{s}_{(i+1)})$.
(4) Calculate $\beta^{\mathrm{PR}}_{\mathrm{C}(i+1)} = \frac{\mathbf{r}^\mathrm{T}_{(i+1)}(\mathbf{r}_{(i+1)} - \mathbf{r}_{(i)})}{\mathbf{r}^\mathrm{T}_{(i)}\mathbf{r}_{(i)}}$ (Polak–Ribiere formula), $\beta_{\mathrm{C}(i+1)} = \max\{\beta^{\mathrm{PR}}_{\mathrm{C}(i+1)}, 0\}$, $\mathbf{h}_{(i+1)} = \mathbf{r}_{(i+1)} + \beta_{\mathrm{C}(i+1)}\mathbf{h}_{(i)}$.
(5) Terminate the algorithm if $\|\boldsymbol{r}_{(i)}\| \leqslant \varepsilon\|\boldsymbol{r}_{(0)}\|$, $\varepsilon < 1$; otherwise, go to step 2.

Note that, in step 2, line search based on the GSS–PI algorithm is performed to choose $\alpha_{\mathrm{C}(i)}$ that maximizes the cost function J along a line. The GSS–PI algorithm is a bracketing method well suited to finding the extremum of a unimodal function. One advantage of the method is that it enables an efficient search for an extremum with a finite number of steps without having to evaluate numerical gradients. Several expressions for the value β_C are equivalent in the linear CG algorithm. However, these expressions are no longer equivalent in the nonlinear CG algorithm. In step 4, the Polak–Ribiere formula [22] is adopted to compute β_C for subsequent numerical simulations. Furthermore, the convergence of the algorithm can be ensured by choosing $\beta_{\mathrm{C}(i+1)} = \max\{\beta^{\mathrm{PR}}_{\mathrm{C}(i+1)}, 0\}$. Using this value is tantamount to restarting CG if $\beta^{\mathrm{PR}}_\mathrm{C} < 0$. To restart CG is to forget the past search direction, and start CG anew in the direction of steepest descent.

In the present energy harvester problem, the cost function we wish to maximize is

$$J = \int_0^{T_\mathrm{p}} \frac{v_\mathrm{p}^2(t)}{R_L}\,\mathrm{d}t, \tag{11}$$

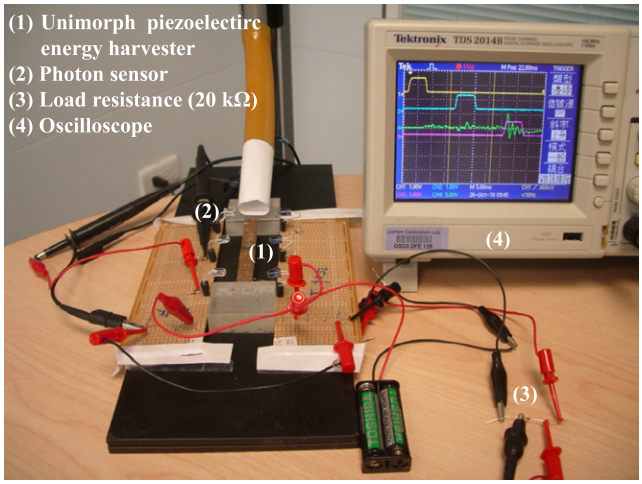

(a)

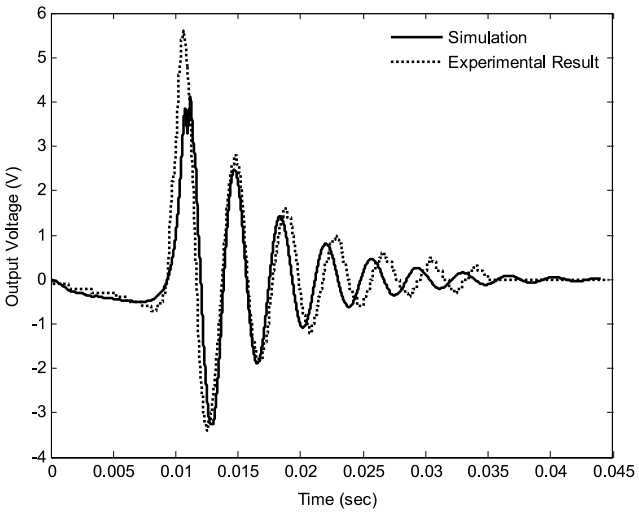

(b)

Figure 3. Experimental result and numerical simulation of the simply supported piezoelectric energy harvester. (a) Experimental arrangement. (b) Comparison of the time response of the output voltage simulation using the FEM and the measurement.

where the T_p is the time duration when the output voltage magnitude is greater than 10 mV, as shown in figure 3(a). Clearly, the cost function J to be maximized is equivalent to the total energy output during the time T_p.

4. Experimental validation and design optimization

This section concerns experimental validation of the FEM and design optimization based on nonlinear CG. The measured voltage response is compared with that predicted by the preceding FEM. The design is optimized for a specified beam length, with the aid of the on nonlinear CG algorithm. The effects of velocity, acceleration, mass ratio and beam length variation on the optimized design are also investigated.

4.1. Experimental validation

Figure 3(a) shows the experimental arrangement for measuring the voltage response of the energy harvester with pinned–pinned supports. The energy harvester is a beam structure

Table 1. Parameters of the piezoelectric ceramic, the substrate and the moving mass used in the experiment.

Material parameters	Phosphor bronze (C5210)	Lead zirconate titanate (PZT-5H)	Glass
Width, W_b (cm)	1	1	—
Thickness t_b (cm)	0.01	0.02	—
Length L (cm)	4	4	—
Density ρ_b (kg m^{-3})	8800	7500	—
Young's modulus, E (GPa)	110	63	—
Strain constant, d_{31} (m V^{-1})	—	-274×10^{-12}	—
Capacitance, c_p (F)	—	30×10^{-9}	—
Moving mass, m (g)	—	—	6.1

Table 2. Parameters of the piezoelectric ceramic and the substrate used in the simulation.

Material parameters	Phosphor bronze (C5210)	Lead zirconate titanate (PZT-5H)
Width, W_b (cm)	1	1
Thickness t_b (cm)	0.1	0.2
Length L (cm)	4–15	4–15
Density ρ_b (kg m^{-3})	8800	7500
Young's modulus, E (GPa)	110	63
Strain constant, d_{31} (m V^{-1})	—	-274×10^{-12}
Capacitance, c_p (F)	—	30×10^{-9}

composed of two layers: a piezoelectric ceramic (PZT-5H) layer and a substrate layer made of bronze (C5210), as previously shown in figure 1. The geometric and material properties of the piezoelectric layer, the substrate layer and the moving mass are summarized in table 1. As shown in figure 3(a), a resistive load of 20 kΩ and a piezoelectric layer electrically connected in series is constructed. The output voltage across the resistive load is measured with an oscilloscope (Tektronix TDS 2014B). In addition, three pairs of photosensors located at the center and the two ends of the energy harvester are utilized to detect the travel time of the moving mass. A marble traveling with velocity 3.6364 m s^{-1} served to excite the energy harvester. In figure 3(b), the measured voltage response is compared with the simulation result obtained using equations (10). As can be seen from figure 3(b), the measurement and the prediction of the voltage responses are in good agreement. The discrepancy of the amplitude and the frequency could be due to the deviation of the real end conditions from the ideal simply supported boundary conditions. In addition, inaccuracy of material constants and numerical errors introduced by the shape functions can also contribute to the discrepancies.

4.2. Optimal design obtained using the nonlinear CG algorithm

In the simulations, the forced vibration response of the piezoelectric energy harvester with pinned–pinned supports subjected to a moving mass is examined. The numerical model is established with eight beam elements ($n = 8$), and the structural damping parameters are taken as $\alpha = 14.65$ and $\beta = 1 \times 10^{-5}$. The physical parameters for the piezoelectric ceramic

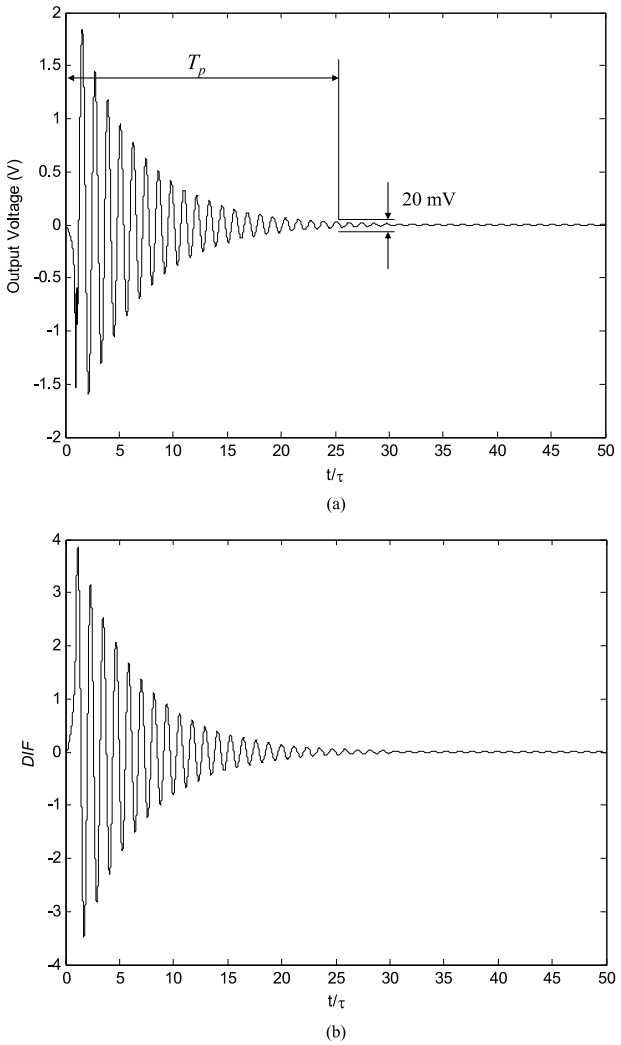

Figure 4. Time history of the displacement impact factor and the voltage output under conditions of constant velocity, $\tau/T_{\rm f} = 0.847$, $\beta_{\rm m} = 3$, $R_{\rm L} = 6$ kΩ, and $L = 7$ cm. (a) Time response of the output voltage, where $T_{\rm p}$ is the time duration with the output voltage magnitude greater than 10 mV. (b) Time response of the displacement impact factor.

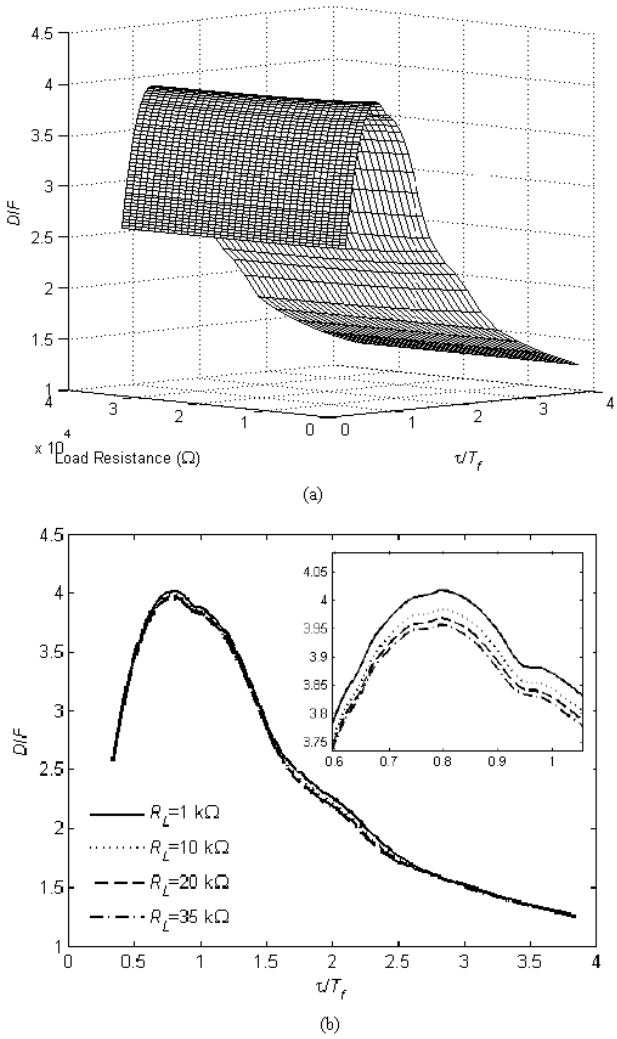

Figure 5. Maximum displacement impact factor under conditions of constant velocity, $\beta_{\rm m} = 3$, and $L = 10$ cm. (a) Performance surface. (b) The displacement impact factor versus various load resistance values $R_{\rm L} = 1$, 10, 20, and 35 kΩ ($\tau/T_{\rm f} = 0.847$).

plate and the substrate are summarized in table 2. Another two parameters are also introduced to aid the subsequent analysis:

$$\beta_{\rm m} = \frac{m}{(\rho_b A_b + \rho_{\rm p} A_{\rm p})L} \tag{12}$$

$$\text{DIF} = \frac{48\delta EI}{mgL^3}. \tag{13}$$

In the expressions above, $\beta_{\rm m}$ denotes the ratio of the moving mass to the beam mass. DIF denotes the displacement impact factor defined as the ratio of dynamic deflection to the static deflection at the midpoint of the beam, with δ representing the dynamic deflection of the beam subjected to the moving mass. In addition, parameters $T_{\rm f}$, t and τ are used in the following simulation to denote the resonant period (reciprocal of the resonant frequency) of the simply supported beam, time and the total travel time of the mass moving from the left end to the right end.

The first simulation examines the transient responses of the voltage output and displacement impact factor (DIF) under the conditions of constant velocity, $\tau/T_{\rm f} = 0.847$, $\beta_{\rm m} = 3$, $R_{\rm L} = 6$ kΩ, $L = 7$ cm. The results are shown in figure 4. Figure 4(a) demonstrates that large stress yields large deformation and hence high effective electrical output. Figure 4(b) reveals that the maximum dynamic deflection is nearly four times the static deflection, which takes place at the instance that the mass leaves the beam [20]. Figure 5(a) shows the maximum displacement impact factor with respect to various travel times and load resistance for the beam length $L = 10$ cm. The maximum displacement impact factors are attained with the same travel time $\tau/T_{\rm f} = 0.781$, irrespective of the load resistance. Furthermore, figure 5(b) shows the maximum displacement impact factors for selected load resistances $R_{\rm L} = 1$, 10, 25 and 35 kΩ. In view of the graph, the curves are indistinguishable for the selected load resistances. However, as can be seen in the enlarged view of figure 5(b), there are considerable variations in the optimum

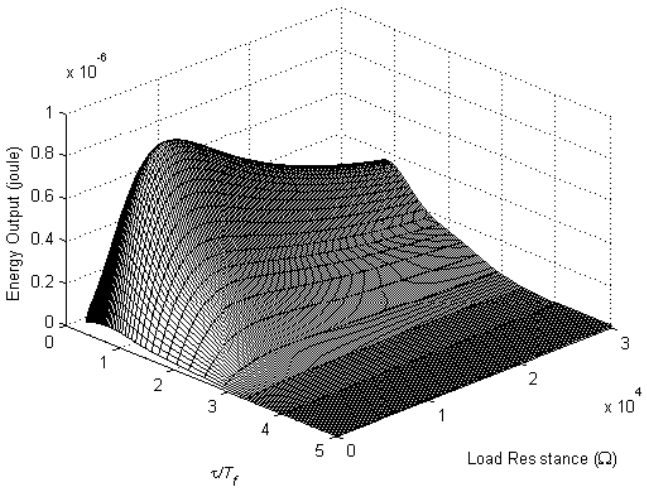

Figure 6. Performance surface of the energy output under the conditions of constant velocity, $\beta_m = 3$, and $L = 7$ cm.

travel time. As the value of the load resistance is increased up to 35 kΩ, the vibration amplitude at $\tau/T_f = 0.781$ declines considerably due to the resistive shunt damping effect [29] on power generation. Dissipation of electrical energy leads to increased effective damping of the system.

In figure 6, the energy output for beam length $L = 7$ cm under the conditions of constant velocity and $\beta_m = 3$ is plotted for various velocity and load resistance values. The trend of energy throughput with respect to load resistance and travel time is not monotonic. The maximum energy output is 8.6256×10^{-7} J when $\tau/T_f = 0.847$ and $R_L = 6$ kΩ. Figure 5(a) reveals that the optimum travel time for the maximum energy output is slightly less than that for the maximum displacement. In addition, the energy output is highly dependent on the load resistance. A unique maximum point can be found on the bowl-shaped energy performance surface (figure 6). It is worth exploring how the optimum energy output varies with respect to various levels of load resistance and travel time for a particular beam length and mass ratio. To this end, the preceding nonlinear CG algorithm is employed to optimize the design parameters of the energy harvester. Figure 7(a) illustrates the convergence history of the cost function using this method. The performance surface and the contour plot are also shown in figures 7(b) and (c), respectively, with the convergence path indicated. As can be seen in the results, it takes only five steps to converge to the maximum point.

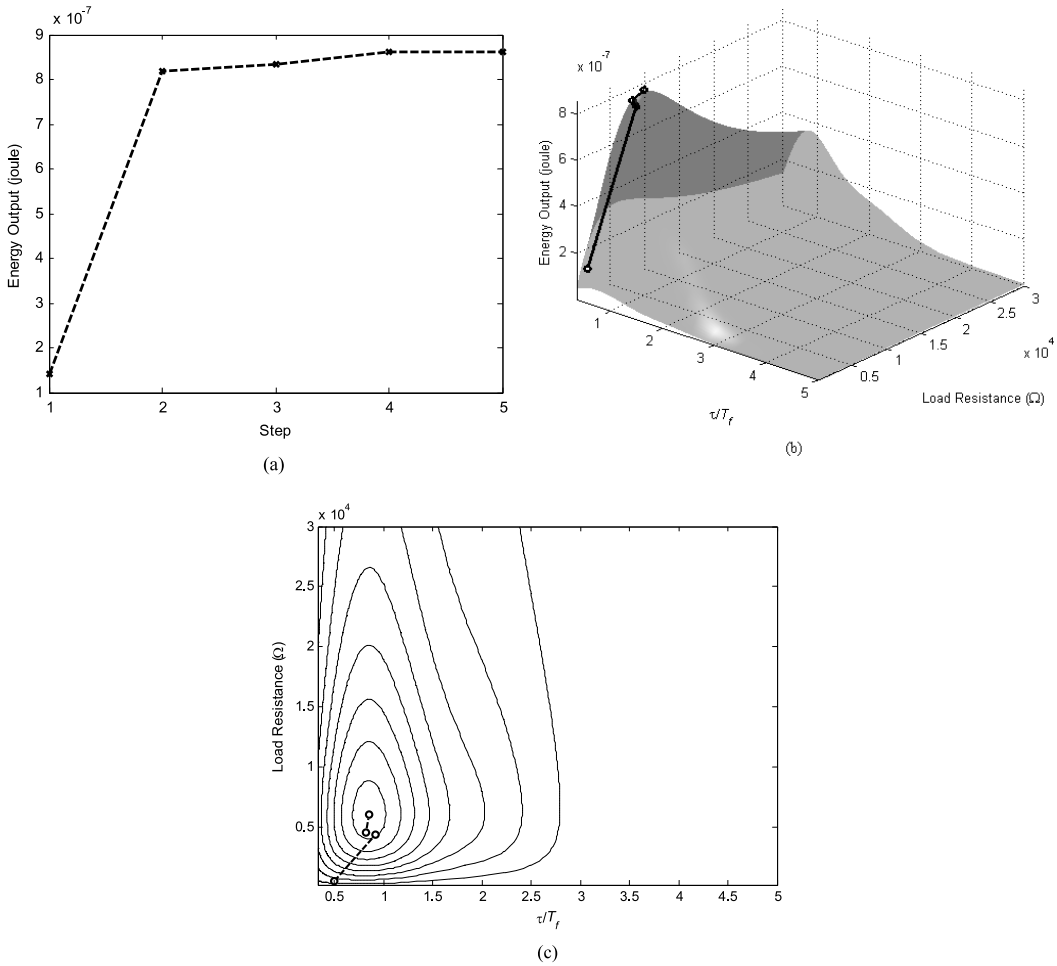

Figure 7. Convergence history of the nonlinear CG algorithm in maximizing piezoelectric energy output under the conditions of constant velocity, $\beta_m = 3$, and $L = 10$ cm. (a) Convergence history of the cost function. (b) Performance surface with the convergence path indicated. (c) Contour plot with the convergence path indicated.

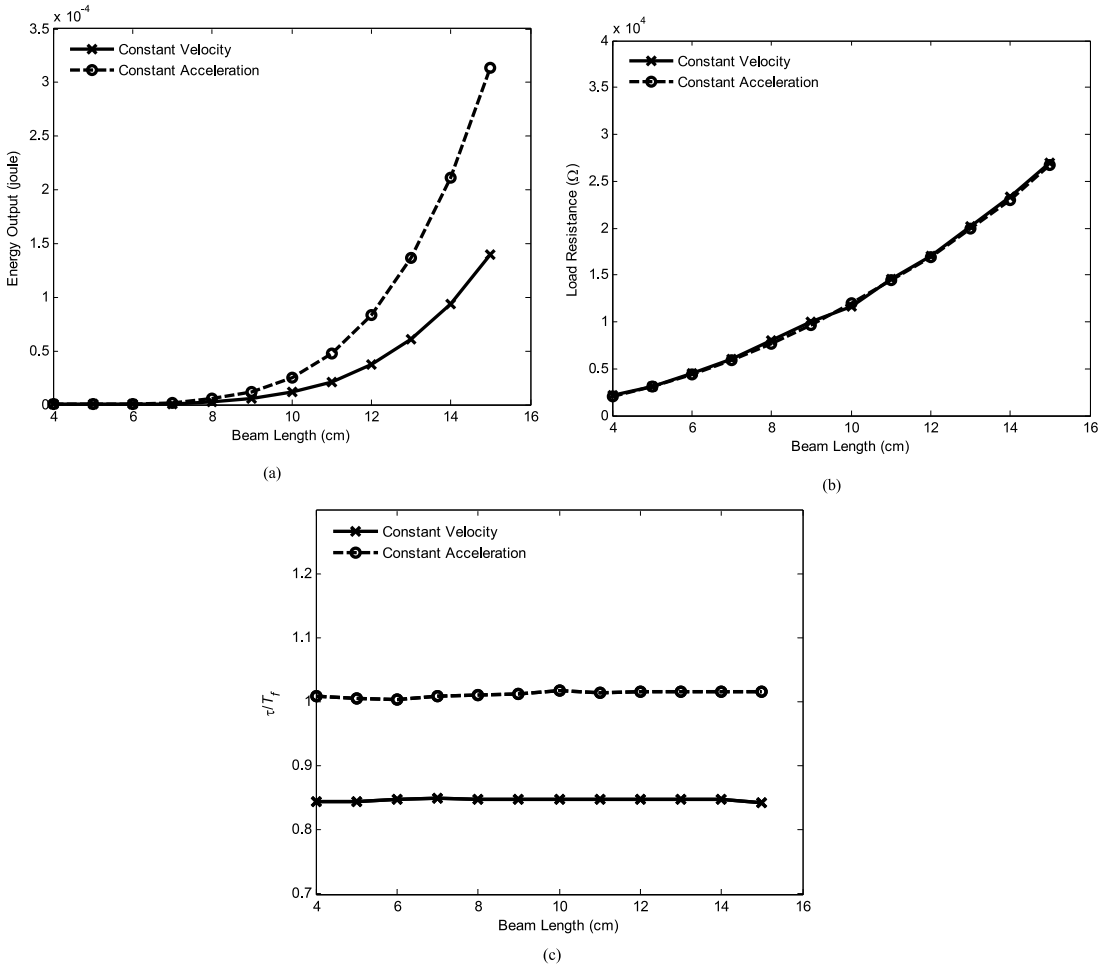

Figure 8. Optimized design of the piezoelectric energy harvester under conditions of constant velocity and constant acceleration, respectively, calculated for various beam lengths. (a) Maximum energy output for various beam lengths. (b) Optimal R_{L} for various beam lengths. (c) Optimal τ/T_{f} for various beam lengths.

Figure 8(a) illustrates the variations of the optimum energy output with respect to various beam lengths, where the curves represent the optimum energy output for different travel speeds. The dashed line and the solid line correspond to the constant acceleration and the constant velocity conditions, respectively. Evidently, the energy output increases with the beam length for both cases because the effective stiffness decreases with the beam span. Moreover, energy throughput in the constant acceleration case is higher because of larger deflection than in the constant velocity case [20], as shown in figure 8(a). Figures 8(b) and (c) show the optimum load resistance and optimum travel time for the energy harvester, respectively. The optimum load resistance increases monotonically with the beam length. Another observation is that the optimum load resistances for the constant acceleration and constant velocity conditions are identical. In figure 8(c), the curves of optimum travel time for constant velocity and constant acceleration for various load resistance values. τ/T_{f} are approximately 0.847 and 1.00 for the constant velocity and the constant acceleration cases, respectively. It is noted that the optimum travel time for constant velocity is shorter than that for constant acceleration.

Figure 9(a) shows the variation of optimum energy output with respect to the beam length for some mass ratios selected ($\beta_{\mathrm{m}} = 1, 3$ and 5). The optimum energy output can be increased by increasing the beam length for any mass ratio. As the mass of the moving object is increased, the energy output is increased. Similar to figures 8(b) and (c), figures 9(b) and (c) show a nearly identical trend of the optimum load resistance for the constant velocity and the constant acceleration cases. Increase in the moving mass entails an increase in the optimum travel time, as evidenced in figure 9(c).

5. Conclusions

In this paper, a finite element model has been derived for a simply supported piezoelectric energy harvester for moving mass induced vibration. The model is based on the Euler–Bernoulli beam theory and serves as the basis for numerical simulations and optimization. Furthermore, the FEM has yielded reasonable predictions in line with experimental results. The nonlinear CG technique is employed to maximize the energy output. The effects of load resistance, travel time of the moving mass and mass ratio have been examined in detail.

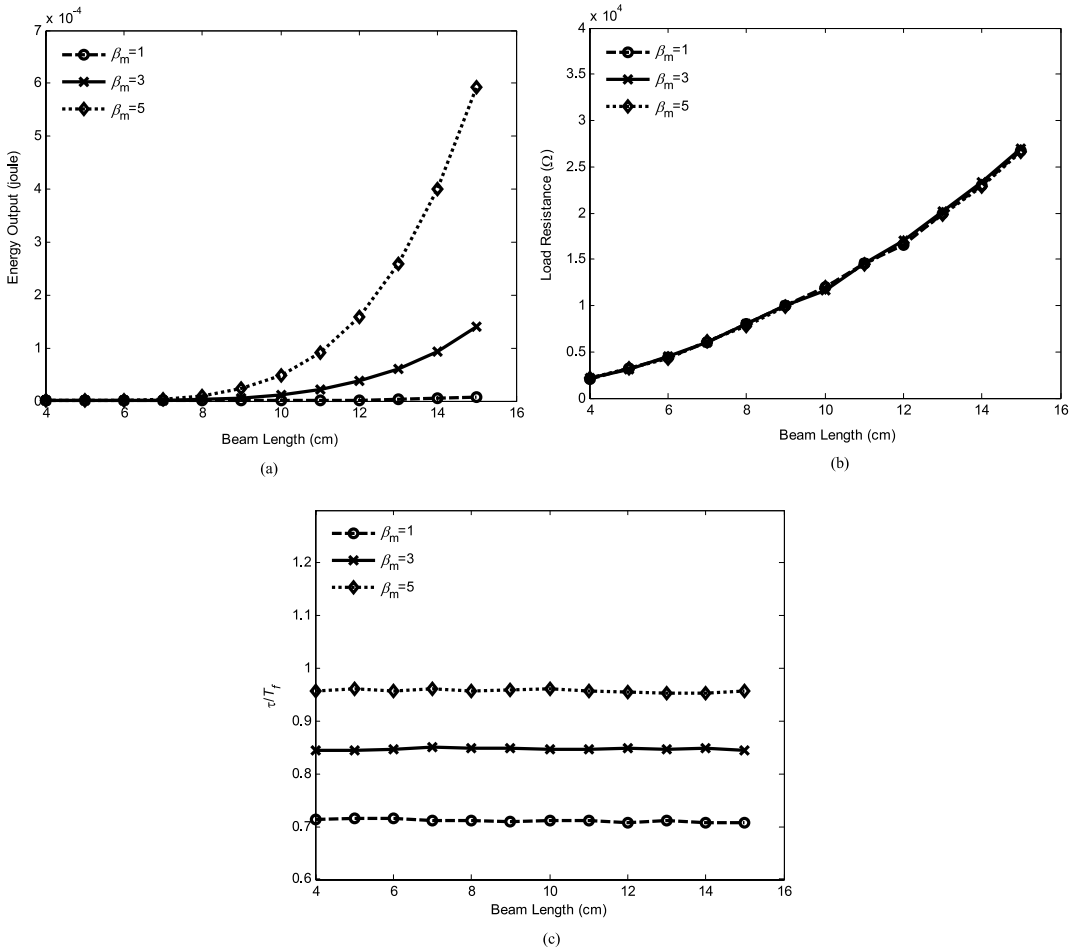

Figure 9. Optimized design for the piezoelectric energy harvester under conditions of constant velocity and $\beta_m = 1, 3, 5$, calculated for various beam lengths. (a) Maximum energy output for various beam lengths. (b) Optimal R_L for various beam lengths. (c) Optimal τ/T_f for various beam lengths.

As evident from the numerical simulations, an optimal energy output of 8.6256×10^{-7} J is obtained when $\tau/T_f = 0.847$ and $R_L = 6$ kΩ under conditions of constant velocity, $\beta_m = 3$ and $L = 7$ cm. This can be contrasted to a non-optimal case where the energy output is 1.967×10^{-7} J obtained with load resistance $R_L = 600$ Ω. The optimal parameters have effectively increased the energy throughput. The results also indicate that load resistance and travel time of the moving mass play an important role in the optimized energy output.

Several aspects of the study remain to be explored in the future. For example, the model can be extended with Timoshenko beam theory, which accounts for the effects of shearing deformations and rotary inertia, and general motion profiles of the mass. Instead of the simple resistor as an electric load, many works have shown that the practical constraints induced by a real electric load may strongly modify the optimal electromechanical parameters. It has been demonstrated that the reactive component of the electrical load can be used to tune the harvesting system to significantly increase the output power off the resonant peak of the device [30]. A vibration-based energy harvester connected to a generalized electrical load is worth exploring for practical applications. Furthermore, nonlinear dynamic analysis for the present structure is also an interesting subject to investigate.

Acknowledgment

The work is supported by the National Science Council in Taiwan, under project number NSC 95-2221-E-009-009-MY2.

References

[1] Arnold D 2007 Review of microscale magnetic power generation *IEEE Trans. Magn.* **43** 3940–51
[2] Zuo L, Scully B, Shestani J and Zhou Y 2010 Design and characterization of an electromagnetic energy harvester for vehicle suspensions *Smart Mater. Struct.* **19** 045003
[3] Mitcheson P, Miao P, Start B, Yeatman E, Holmes A and Green T 2001 MEMS electrostatic micro-power generator for low frequency operation *Sensors Actuators* **115** 523–9
[4] Aton S R and Sodano H A 2007 A review of power harvesting using piezoelectric materials (2003–2006) *Smart Mater. Struct.* **16** R1–21
[5] Wang L and Yuan F G 2008 Vibration energy harvesting by magnetostrictive material *Smart Mater. Struct.* **17** 045009
[6] Carmo J P, Goncalves L M and Correia J H 2010 Thermoelectric microconverter for energy harvesting systems *IEEE Trans. Ind. Electron.* **57** 861–7

[7] Sodano H A and Inman D J 2004 A review of power harvesting form vibration using piezoelectric materials *Shock Vib. Dig.* **36** 197–205
[8] Harb A 2010 Energy harvesting: state-of-the-art *Renew. Energy* at press (doi:10.1016/j.renene.2010.06.014)
[9] Umeda M, Nakamura K and Ueha S 1996 Analysis of the transformation of mechanical impact energy to electric energy using piezoelectric vibrator *Japan. J. Appl. Phys.* **35** 3267–73
[10] Roundy S, Wright P and Rabaey J 2003 A study of flow level vibration as a power source for wireless sensor nodes *Comput. Commun.* **26** 1131–44
[11] du Toit N E, Wardle B L and Kim S G 2005 Design consideration for MEMS-scale piezoelectric mechanical vibration energy harvesters *Integr. Ferroelectr.* **71** 121–60
[12] Ajitsaria J, Choe S Y, Shen D and Kim D J 2007 Modeling and analysis of a bimorph piezoelectric cantilever beam for voltage generation *Smart Mater. Struct.* **16** 447–54
[13] Erturk A and Inman D J 2008 Issues in mathematical modeling of piezoelectric energy harvesters *Smart Mater. Struct.* **17** 065016
[14] Hagood N W, Chung W H and Von F A 1990 Modeling of piezoelectric actuator dynamics for active structural control *J. Intell. Mater. Syst. Struct.* **1** 327–54
[15] Lu F, Lee H and Lim S 2004 Modeling and analysis of micro piezoelectric power generators for micro-electromechanical-systems applications *Smart Mater. Struct.* **13** 57–63
[16] Erturk A and Inman D J 2008 A distributed parameter electromechanical model for cantilevered piezoelectric energy harvesters *ASME J. Vib. Acoust.* **130** 041002
[17] De Marqui C Jr, Erturk A and Inman D J 2009 An electromechanical finite element model for piezoelectric energy harvester plates *J. Sound Vib.* **327** 9–25
[18] Challa V R, Prasad M G, Shi Y and Fisher F T 2008 A vibration energy harvesting device with bidirectional resonance frequency tenability *Smart Mater. Struct.* **17** 015035
[19] Wickenheiser A M and Garcia E 2010 Broadband vibration-based energy harvesting improvement through frequency up-conversion by magnetic excitation *Smart Mater. Struct.* **19** 065020
[20] Lin Y H and Trethewey W 1990 Finite element analysis of elastic beams subjected to a moving dynamic loads *J. Sound Vib.* **136** 323–42
[21] Newmark N M 1959 A method of computation for structure dynamic *ASCE Eng. Mech. Div.* **85** 67–94
[22] Daniel J W 1967 Convergence of the conjugate gradient method with computationally convenient modifications *Numer. Math.* **10** 125–31
[23] Fletcher R and Reeves C M 1964 Function minimization by conjugate gradients *Comput. J.* **7** 149–54
[24] IEEE Group on Sonics and Ultrasonics 1978 *IEEE Standard on Piezoelectricity* (New York: IEEE)
[25] Cook R D, Malkus D S and Plesha M E 1989 *Concepts and Applications of Finite Element Analysis* (New York: Wiley) pp 95–101
[26] Meirovitch L 1986 *Elements of Vibration Analysis* (Singapore: McGraw-Hill) pp 210–4
[27] Gere J M and Timoshenko S P 1984 *Mechanics of Materials* (Belmont, CA: Wadsworth) pp 249–57
[28] Brent R P 1973 *Algorithm for Minimization without Derivatives* (Englewood Cliffs, NJ: Prentice-Hall) pp 48–75
[29] Lesieutre G A, Ottman G K and Hofmann H F 2004 Damping as a result of piezoelectric energy harvesting *J. Sound Vib.* **269** 991–1001
[30] Cammarano A, Burrow S G, Barton D A W, Carrella A and Clare L R 2010 Tuning a resonant energy harvester using a generalized electrical load *Smart Mater. Struct.* **19** 055003